JMEPEG (2016) 25:4521–4528
DOI: 10.1007/s11665-016-2275-1

1059-9495/$19.00

Evaluation of the Particle Bonding for Aluminum Sample Produced by Spark Plasma Sintering

Mehmet Masum Tünçay, Lucie Nguyen, Philippe Hendrickx, and Mathieu Brochu

(Submitted April 20, 2016; published online August 5, 2016)

Spark plasma sintering (SPS) is a powder metallurgy process that sinters powder materials within a short time by simultaneous application of electrical current and pressure. SPS differs from other conventional powder metallurgy processes by its heating mechanism, which is Joule heating of the sample within a graphite die. This study investigates the consolidation of aluminum powder by SPS. Different pressures were used and particle bonding evaluated by means of fracture surface analysis. Electrical resistance, obtained from online monitoring of the variation of voltage and current during the process, showed an enhanced descent at 0.3 T_m, and the area under this drop was associated with ductility: the greater the area, the higher the ductility. This temperature corresponds to a significant increase in the hardness ratio of the oxide layer to aluminum, where breakdown of the oxide layer becomes easier, permitting enhanced metallurgical bonding between the powder particles.

Keywords aluminum, oxide, particle bonding, powder metallurgy, resistance, spark plasma sintering

1. Introduction

Spark plasma sintering (SPS), also called field-assisted sintering, is a powder metallurgy (P/M) process that uses uniaxial pressure and pulsed direct electrical current to perform rapid powder consolidation. It differs from conventional P/M processes by its heating mechanism: Joule heating. Heat arises from the electrical current that flows through the die-punch-conductive powder assembly during the process. SPS provides high heating rates and short processing times (Ref 1), yielding dense compacts (Ref 2).

Aluminum (Al) possesses a native oxide film and is hard to sinter by conventional P/M processes (Ref 3). Munir (Ref 4) showed that the presence of stable surface oxides at high temperatures and limited oxide solubility in the metal particles can result in retardation of sintering such that it requires an incubation time. For Al particles having a 100 Å thick oxide layer, the incubation time is around 116 days at 873 K (Ref 4). Therefore, sintering of Al requires creating metal-to-metal contact by disrupting their surface oxide layers. Thus, SPS becomes an attractive process for sintering of Al particles; this is supported by several studies, the main outcomes of which are detailed below.

- Xie et al. (Ref 5) carried out SPS on Al powder and observed that the tensile strength of the sintered compact is comparable with base Al metal for the following sintering conditions: 823 K at 47 MPa and 873 K at 23.5 MPa. However, the ductility of the former was lower than that of the base metal, suggesting that a higher temperature improves metal/metal bonding, creating higher ductility.
- Nagae et al. (Ref 6) compared the sintering of Al powder by pulsed current sintering (PCS) and simulated hot pressing (HP)—i.e., operating the PCS at a heating rate of 18 K/min. They reported improved tensile properties for PCS sintered gas-atomized Al powder compared to the simulated hot pressed. The authors suggested that use of Joule heating to preferentially heat interfacial regions of particles could improve break-up of the oxide layer during PCS.
- Xie et al. (Ref 7) sintered pure Al by pulse electrical current sintering (PECS) at various pulse frequencies and found that relative density, electrical resistivity and tensile properties was not significantly affected by pulse frequency.
- Xie et al. (Ref 8) discussed the breakdown mechanism of the oxide layer of Al during PECS through the fractions of metal/metal bonding interfaces for a sintered specimen using high-resolution TEM. The improvement in bonding, associated with the plastic deformation during compaction, led the authors to speculate that the high-temperature contact points of PECS will favor oxide breakdown relative to hot pressing.
- Zadra et al. (Ref 9) showed that the application of pressure at higher temperatures improves ductility so that the neck growth between powder particles and the electric current supports uniform sintering resulting in better ductility.
- Kwon et al. (Ref 10) observed that oxide layer debris created improved metal-to-metal contact upon SPS. They also carried out O_2 content analysis and found a lowering of the content with increasing sintering temperature that was associated with the generation of microplasma between particle contacts, pressure and reduced atmosphere that comes from carbon mold.

Mehmet Masum Tünçay, Department of Mining and Materials Engineering, McGill University, 3610 University Street, Montreal, QC H3A 0C5, Canada; and Department of Metallurgical and Materials Engineering, Marmara University, 34722 Goztepe, Istanbul, Turkey; and **Lucie Nguyen, Philippe Hendrickx,** and **Mathieu Brochu**, Department of Mining and Materials Engineering, McGill University, 3610 University Street, Montreal, QC H3A 0C5, Canada. Contact e-mail: mathieu.brochu@mcgill.ca.

- Finally, Sweet et al. (Ref 11) showed that SPS of Al resulted in a reduced oxygen content in the sintered compact. That behavior was not observed during conventional sintering trials. Correspondingly, tensile elongations reaching up to 32.7% was reported, a value comparable with 1xxx wrought alloys in an annealed condition. In comparison, tensile elongation of 0.4% was reported for conventional P/M process.

These outcomes suggest that the interacting factors influencing the sintering of Al powders are temperature and plastic deformation, which directly affect the oxide breakdown and improve the bonding quality. In this context, this study aims to detect the oxide layer breakdown through the evolution of variation in resistance by online monitoring of voltage and current data of SPS during densification, and by linking this behavior to ductility. Bulk densities of sintered compacts were evaluated by the Archimedean method. A three-point bending test was applied to investigate the ductility of the samples, and fracture surface analysis was carried out using SEM to evaluate the particle bonding. Comparisons between resistance profiles and fracture surfaces are made to assess interface quality.

2. Experimental

Experiments were performed using gas-atomized Al (H-15) powder supplied by Valimet (Stockton, CA). Chemical composition of the powder is listed in Table 1, per the supplier's certificate of analysis. Particle size distribution (PSD) of the powder was measured using a HORIBA LA-920 laser diffraction particle size analyzer according to ASTM B822-02. D_{10}, D_{50} and D_{90} of the powder are given in Table 2. An SEM image of the initial powder is shown in Fig. 1. The oxide layer of the powder was investigated using transmission electron microscopy (TEM) with an FEI Tecnai G2 F20 transmission electron microscope operated at 200 kV, as shown in Fig. 2. The oxide layer thickness was approximately 4 nm.

SPS was carried out under vacuum with an SPS 10-3 apparatus (Thermal Technologies Inc., Santa Rosa, CA). Cylindrical samples were produced using 50 g of powder with a 38 mm diameter graphite die-punch set (Isocarb Graphite I-85, Electrodes Inc., Sante Fe Springs, CA). Graphite foil with a thickness of 0.13 mm was used between the sample-punch and upper spacer-upper electrode. The sintering cycle consisted of heating samples at 100 °C/min up to 500 °C (0.75 T_m homologous temperature) and then holding them at 500 °C for 1 min. One of four different pressures (20, 30, 40 and 50 MPa) was applied to a sintering cycle. Al samples were also produced using 20 MPa pressure followed by 50 MPa pressure at the end of the process, during the cooling period (this procedure will be referred to as 20-50 MPa hereafter). In addition, the same sintering cycle with 50 MPa was applied to a near fully dense Al sample in order to have the reference resistance versus homologous temperature profile. Three samples were produced for each condition. The dimensions of each component of the SPS setup are provided in Table 3.

The bulk density of the samples was measured using Archimedes' method as described in ASTM standard B963-13. Resistance profiles of each sintering cycle were obtained by dividing voltage with electrical current data during SPS. The estimated resistance during the process was determined using Eq 1-3 and procedure described below.

Table 1 Chemical composition of the powder

	Elements (wt.%)	
Material	**Al**	**Fe**
Al (H-15)	99.8	0.11

Table 2 PSD of the powder

D_{10} (μm)	10
D_{50} (μm)	21
D_{90} (μm)	45

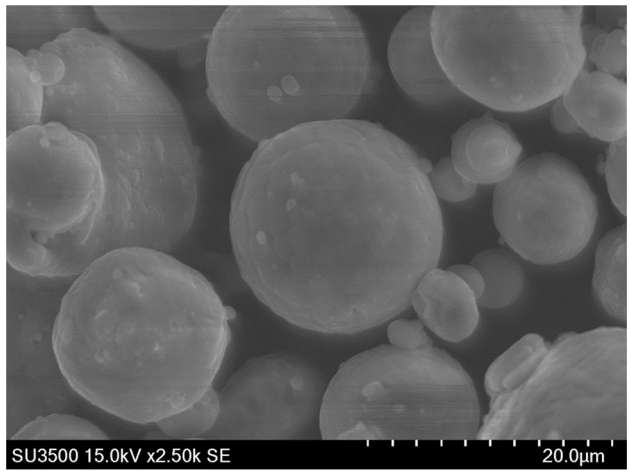

Fig. 1 SEM image of Al (H-15) powder particles

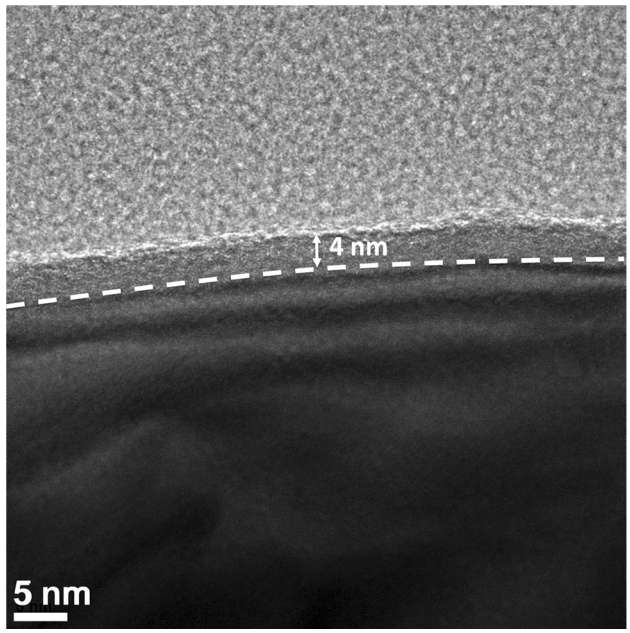

Fig. 2 Transmission electron micrograph of Al (H-15) powder particle

Table 3 Dimensions of the parts

Part	Diameter (mm)	Height (mm)
SS upper electrode	59	500
SS lower electrode	59	250
Spacers	59	45
Upper punch	37.7	45.3
Lower punch	37.7	36.2
Die	38 (inner) 73 (outer)	46
Near fully dense Al	37.7	16.7

Table 4 Electrical resistivity values

Material	Electrical resistivity, Ω m (T in K)
AISI 304 SS (Ref 13)	$7 \times 10^{-18}T^4 - 3 \times 10^{-14}T^3 + 5 \times 10^{-11}T^2 - 4 \times 10^{-8}T + 2x10^{-5}$
Graphite (Ref 14)	$1/(3/(6.083 \times 10^{-6} + 1.4585 \times 10^{-6}T/1000 + 2.3568 \times 10^{-6}/T/1000))$
Al (Ref 15)	$1 \times 10^{-10}T - 8 \times 10^{-9}$
Graphite foil (Ref 12)	2.5×10^{-3}

Resistance of a part can be calculated using Eq 1 (Ref 12):

$$R = \rho h/A \quad \text{(Eq 1)}$$

where R is the resistance in ohms (Ω), ρ is the resistivity in Ω/m, h is the height in m and A is the cross-sectional area in m^2. The electrical resistivity values (Ref 12-15) used during the calculations are given in Table 4. Since a water cooling system was used for the stainless steel electrodes, room temperature resistivity was used for the electrodes.

In the SPS setup, resistance also comes from the contact between parts (Ref 16). Wei et al. (Ref 17) estimated temperature- and pressure-dependent equations for horizontal and vertical contact resistance in the SPS tooling setup based on the regression analysis of experimental results:

$$R_h(T,P) = (-0.24 \cdot \ln T + 1.94) \cdot \left(27.61 \cdot P^{-1.09}\right) \left[\text{m cm}^2\right] \quad \text{(Eq 2)}$$

$$R_v(T,P) = (-0.0057 \cdot T + 18.59) \cdot (-0.0079 \cdot P + 1.14) \left[\text{m cm}^2\right] \quad \text{(Eq 3)}$$

where T is the temperature (°C), P is the pressure (MPa), and R_h and R_v represent the horizontal and vertical contact resistance, respectively. Resistance that comes from the contact between parts can be obtained by dividing Eq 2 and 3 with the area of contact.

Three-point bending tests (sample dimensions: 2.5 mm × 7 mm × 37 mm) were carried out using a Tinius Olsen H25K-S Instron with a crosshead loading speed of 10 mm/min and a support span of 18.75 mm. The flexural stress, σ_f, in MPa, was obtained using:

$$\sigma_f = 3PL/2wt^2 \quad \text{(Eq 4)}$$

where P is the load in Newtons, L is the span between two sample support beams in mm, w is the width and t is the thickness of the sample in mm. The flexural strain, ε_f, was obtained using:

Table 5 Final densities of the sintered compacts

Sample, MPa	Relative density
20	0.925 ± 0.004
30	0.952 ± 0.004
40	0.966 ± 0.005
50	0.984 ± 0.006

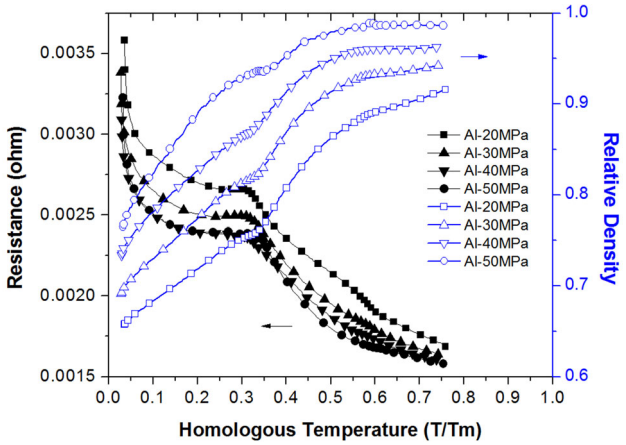

Fig. 3 Variation of resistance and relative density with homologous temperature

$$\varepsilon_f = 6Dt/L^2 \quad \text{(Eq 5)}$$

where D is the maximum deflection at the center of the sample in mm. Three-point bending sample tests were done for each condition, and errors estimated through calculations of the standard deviation. Fracture surface observations were performed with a Hitachi SU-3500 scanning electron microscope.

3. Results and Discussion

3.1 Effect of Pressure

The density of the compacts, expressed as a fraction of the theoretical density (2.7 g/cm^3), is given in Table 5. As expected, with an increase in pressure, the final density of the material approaches the theoretical density.

Figure 3 presents the resistance and relative density behavior as a function of homologous temperature at different pressure conditions. High resistance occurs during the initial stage of the process and decreases as the material densifies, reaching a saturated value for higher-density samples. Furthermore, descent in resistance is enhanced after 0.3 T/T_m. What follows is our interpretation of the mechanisms leading to this observed phenomenon.

SPS differs from hot pressing by its Joule heating mechanism, defined as the heat generated from resistance to the electrical current. During SPS of metal powders, the majority of current flow is through the punch-sample assembly (Ref 12). Hence, the total current can be assumed to pass through the punches and sample (Ref 12). Therefore, the main locations of

Joule heating are the punches, the sample and the graphite foils between the punches and the sample (Ref 12). Following the methodology presented by Chawake et al. (Ref 12), we calculated resistance using Eq 1 for each part (electrodes, spacers, punches, foils and Al sample) and Eq 2 and 3 for the addition of contact resistances.

Electrical resistance that is provided by the densifying component: To calculate the resistance of the powder Al sample, the electrical resistivity of bulk Al (Table 4) was used in the equation for porosity-dependent electrical resistivity (Ref 18):

$$\rho = \rho_0\left[\left(1 + 11\theta^2\right)/(1-\theta)\right] \quad \text{(Eq 6)}$$

where ρ is the resistivity of porous material, ρ_0 is the resistivity of bulk material and θ is the porosity. Combining Eq 6 with Eq 7 (Ref 12) gives:

$$R_{\max} = \rho h_i / A \quad \text{(Eq 7)}$$

where h_i is the instantaneous height of the sample and A is the cross-sectional area, and the predicted maximum electrical resistance (R_{max}) provided by the sample was 1.0×10^{-6} Ω.

The electrical resistance provided by a fully dense Al sample during the whole sintering cycle was also calculated using Eq 1, where the height was 16.7 mm. The total resistance was obtained by summation of the calculated resistance of each component. The effect of the calculated resistance that comes from the Al sample, for both the powder and the near fully dense case, was negligible in comparison with the other components.

Figure 4 shows the resistance versus homologous temperature behavior during a 50 MPa sintering cycle for Al powder, a near fully dense Al sample and the calculated total value. Xie et al. (Ref 8) demonstrated that a fully dense sintered Al powder compact, where bonding between metal particles occurs, has an electrical resistivity similar to bulk Al. Montes et al. (Ref 19) showed that the electrical conductivity of bulk aluminum and fully dense aluminum samples are alike. Therefore, it can be assumed that the total resistance of the sintering cycle for the near fully dense sample run came from

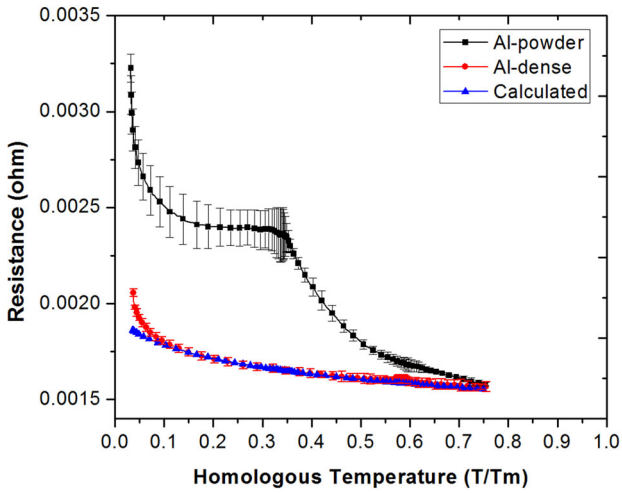

Fig. 4 Resistance vs. T/T_m of aluminum powder, a near fully dense aluminum sample and the calculated total value for 50 MPa sintering cycle

the electrodes-spacers and punches only, as the resistivity of bulk Al at 10^{-8} Ω/m is about two orders of magnitude smaller than that of graphite, at 10^{-6} Ω/m, respectively. The calculated resistance agreed with the experimental resistance curve of a dense Al sample (Fig. 4). The resistance profile of the powder Al sample ended up with the similar value to that of the dense Al sample and the calculated resistance. This is in agreement with the work of Chawake et al. (Ref 12); as the metallic material densifies, the major contribution to the saturated resistance comes from the graphite parts. Based on this observation, the different behavior of the resistance curve of powder Al samples comes from the powder. From the above analyses, the maximum electrical resistance provided by the densifying component was 1.0×10^{-6} Ω. However, this value was negligible in comparison with the resistance values in Fig. 4. Chawake et al. (Ref 12) proposed that an additional electrical resistance component is attributable to the presence of the initial oxide layer on the surface of metallic particles. In that study (Ref 12), Ni powder had an initial resistance was 1.5×10^{-2} Ω. This system showed an enhanced densification at 0.4 T_m which corresponds to the dielectric breakdown of the Ni particles' oxide layer [6×10^5 V/cm (Ref 20)] under an electrical field. Thereafter, the resistance started to reach a saturated value (3.0×10^{-3} Ω), after which it was coming from the graphite parts. Montes et al. (Ref 21) demonstrated that a powder mass having a porosity of 35%, formed by Al powders with 22.2 μm mean particle radius and a 4.5 nm thick oxide layer, had an electrical resistivity of approximately 10^{-3} Ω/m at room temperature. Using Eq 6, which does not take into account the effect of surface oxides, the resistivity of an Al powder bed with 35% porosity is on the order of 10^{-8} Ω/m. Therefore, powders coated with surface oxides provide higher resistance.

During field-assisted sintering, amplification in local field strengths is expected (Ref 22). If the local field strength is greater than the dielectric breakdown strength of the surface oxide, the oxide surface may break down. Bonifacio et al. (Ref 23) showed dielectric breakdown of the surface oxide of Ni powder particles with the help of in situ TEM experiments during electric field-assisted sintering. Although an increase in local field strength is possible during SPS, it is not clear whether it can reach the dielectric breakdown strength of Al oxide [$\sim 1 \times 10^7$ V/cm[1] (Ref 24)] which is two orders of magnitude greater than that of nickel oxide [6×10^5 V/cm (Ref 20)]. An in situ TEM analysis similar to the study of Bonifacio et al. (Ref 23) is required for Al particles to better investigate whether the dielectric breakdown of the surface oxide film can occur. Mechanical disruption of the surface oxides of Al powder during plastic deformation is one way to break the oxide layer (Ref 25). Previous work suggests that it is much easier to break up oxide film on Al at higher temperatures (Ref 26).

Al powder has an inherent oxide layer, and thus resistance profiles and fracture surface analysis can also be used to evaluate whether breakdown of the oxide layer is occurring and how applied pressure influences the breakdown. This understanding is critical, as the inability to break down the oxide layer will yield incomplete, or complete absence of particle bonding between metal particles (Ref 27), resulting in low ductility and brittle fracture (Ref 28).

Initial resistance during SPS of metallic powders, such as Cu and Fe, decreases with the progress of densification (Ref

29). This change in resistance is mostly attributable to the creation of a metal-to-metal contact area between powder particles by the breakdown of the oxide film (Ref 29). As the fraction of metal/metal bonding increases, reduction in the resistance becomes higher (Ref 5). The densification rate is high at the initial stage, and slows as the material densifies (Ref 30). Figure 3 reveals that resistance decreases as densification progresses. Moreover, the change in the resistance increases significantly after 0.3 T_m, and densification is enhanced. This observation of enhanced densification and decreased resistance

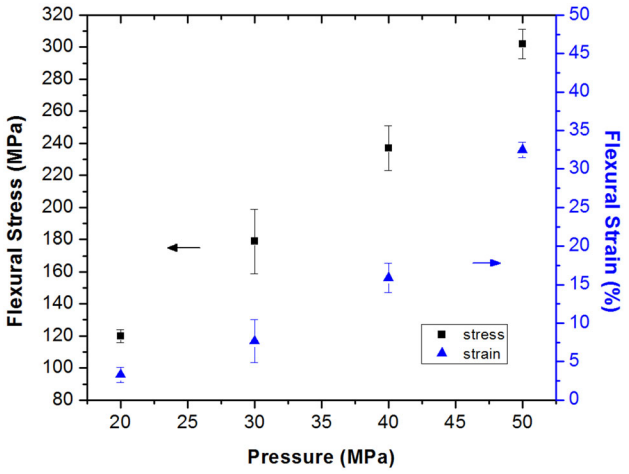

Fig. 5 Three-point bending test results of the different pressure samples

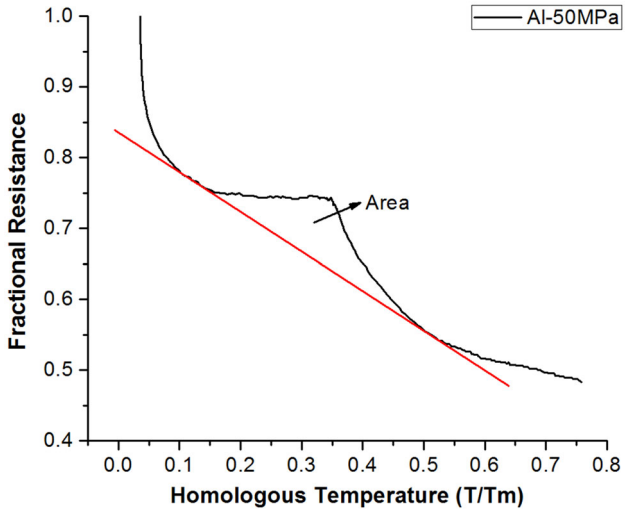

Fig. 7 Fractional resistance vs. homologous temperature curve

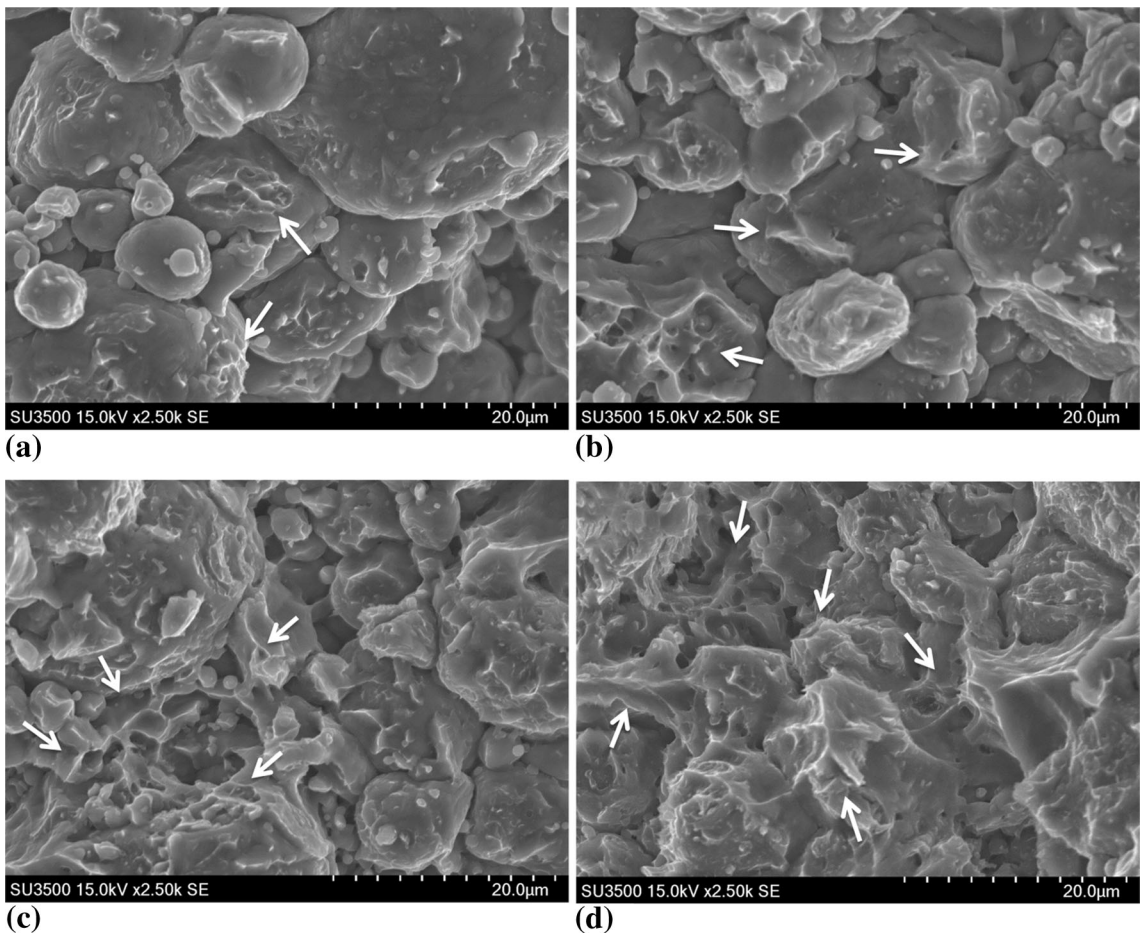

Fig. 6 Fracture surfaces of the samples (arrows point out dimple regions): (a) 20 MPa, (b) 30 MPa, (c) 40 MPa, (d) 50 MPa

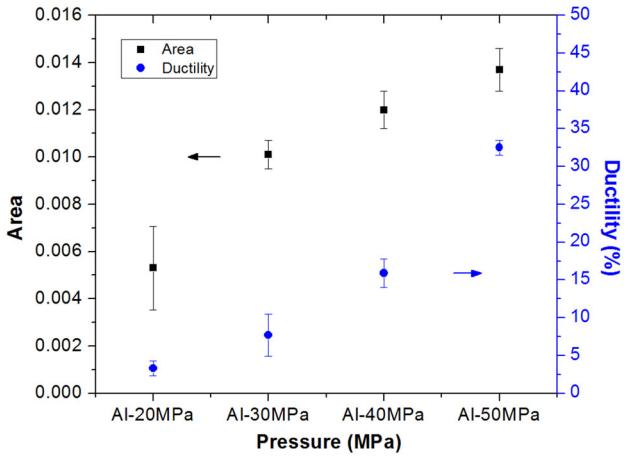

Fig. 8 Area vs. ductility values for the different pressure samples

at ~0.3 T_m can be connected to the breakdown of the oxide layer leading to the formation of high amounts of metal/metal bonding. Tylecote (Ref 26) demonstrated that the hardness ratio of Al_2O_3 to Al increases with an increase in temperature and that a significant change in this ratio occurs above 200 °C, associated with the softening of Al. Hence, it is easier to break up oxide film on Al above this temperature (Ref 26). The temperature where this rise in hardness ratio was observed corresponds to 0.3 T_m, and matches the temperature at which a significant reduction in resistance was observed in this study.

To support the oxide breakdown evidence presented above, three-point bending tests were performed for each sample to assess the ductility of the samples. Fracture surfaces were examined using SEM for any indication of dimples as a sign of plastic behavior, i.e., particle bonding. In particular, the relationship between resistance profiles and fracture surfaces showing particle bonding, ascribed to the breakdown of the oxide layer, is considered. Figure 5 shows the flexural strength and strain values. Corresponding fracture surface micrographs are presented in Fig. 6. Flexural stress and ductility of the samples were enhanced by an increase in pressure (Fig. 5), which is indicative of good particle bonding between metal particles.

Looking at fracture surfaces, the occurrence of particle debonding at 20 MPa can be readily observed, and some small dimple formations (neck development) occur on the particle surfaces. At 30 MPa, a similar behavior was observed with more pronounced dimples that still remain minor. These dimple formations are characteristic of metal-to-metal bonding. At 40 MPa, prior particle boundaries began to disappear and dimple formations are enhanced. The 50 MPa sample exhibit a significant presence of dimples, which supports the occurrence of particle bonding. It is expected that additional oxide layer disruption will occur with an increase in applied pressure. Except from less porosity, the better ductility, and thus bonding, at higher pressures is likely the result of both greater oxide layer disruption and greater consolidation between metal-to-metal contacts.

Oxide layer disruption, (i.e., good bonding and better ductility) was further analyzed by plotting fractional resistance and homologous temperature of the samples. Figure 7 shows a representative graph using a 50 MPa sample. If the area between the tangent line and the curve (as shown in Fig. 7) is calculated, a relationship with the ductility (flexural strain) of the samples can be made. Figure 8 presents the ductility and area values of different pressure samples. The increase in the area was attributed to greater oxide layer disruption. As the area increases, the ductility increases and better ductility is ascribed to better bonding between particles through greater metal-to-metal contact. However, the residual porosity also affects mechanical properties (Ref 31). Therefore, similar density samples may be required to better comment on the relationship between oxide layer breakdown and good bonding. The next section will be used for this purpose.

Table 6 Relative densities of the samples

Sample, MPa	Relative density
20-50	0.961 ± 0.002
40	0.966 ± 0.005

Table 7 Three-point bending test results and the calculated area of similar density samples

Sample, MPa	Flexural stress, MPa	Flexural strain, %	Area
20-50	182 ± 16	6.6 ± 1.9	0.0051 ± 0.0015
40	237 ± 14	15.9 ± 1.9	0.0120 ± 0.0008

3.2 Comparison of Similar Density Samples

To increase the final density of the sample, 20 MPa sample was pressed up to 50 MPa during cooling period. Table 6 shows the final densities (as a fraction of the theoretical density) of 20–50 and 40 MPa sample. Both samples have similar densities. Table 7 shows three-point bending test results and the calculated area of both sample types, and it reveals that the 40 MPa sample has a higher ductility than the 20–50 MPa sample. This is a sign of better metal-to-metal bonding, since the samples have similar densities. The area is higher for the 40 MPa sample where the ductility is also higher. These observations suggest that deviation of the current curve can be used to assess the quality of the interface between Al particles: the greater the area, the better the quality of the interface. Moreover, dimple formations are more pronounced for the 40 MPa sample, as indicated by fracture surfaces (Fig. 9).

The reported good necking quality of SPS Al samples in the literature (Ref 5-11) indicates that SPS has a positive effect on neck development. Pressure is considered as an important parameter to disrupt the oxide layer during SPS of Al powder (Ref 8). Similar to Xie et al. (Ref 8), we believe that oxide breakdown during SPS of Al comes mainly from the plastic deformation and that the effect of the pressure should be amplified by the application of current, which results in Joule heating as a self-heating mechanism within the powder bed. Furthermore, in a study (Ref 9) where the pressure was ramped up during heating, as opposed to before heating as done in this study, improved ductility was observed and associated to the fact that the material was subjected to higher electrical field due to the lower powder density. Hence, it allowed improved mobility of atoms and diffusion (Ref 9). The authors also

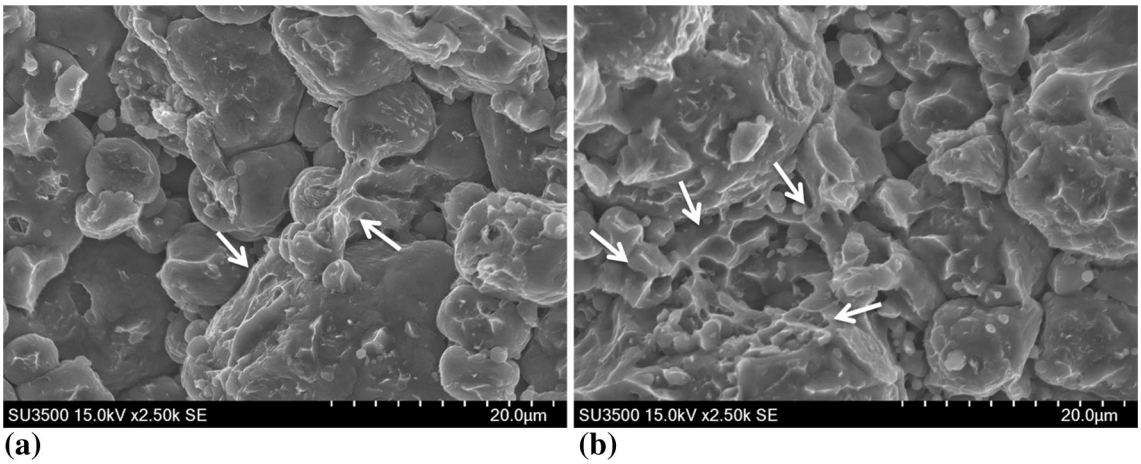

Fig. 9 Fracture surfaces of the similar density samples (arrows point out dimple regions): (a) 20-50 MPa, (b) 40 MPa

suggest that loose powder allows a better surface cleaning of the powder, because of a greater possibility of sparks and/or higher local temperatures between particles and that minimization of gas entrapment with ramping pressure improves plasticity (Ref 9). Enhanced ductility with ramping pressure, in comparison to constant pressure, reveals the aid of electrical current (Ref 9). This self-heating and possible formation of localized high temperatures at the particle contacts (Ref 32) would help to break down the oxide layer by mechanical pressure as the material will be softer and thus can be more effectively deformed. Nagae et al. (Ref 6) report better tensile properties for pulsed electric current sintered gas-atomized Al powder than for hot-pressed ones. They attribute this enhancement of tensile properties to the effect of Joule heating. From these observations, it can be concluded that pressure is important in breaking down the oxide layer during the SPS of Al, but that an electrical field, which is inherent to SPS, may also help to disrupt the oxide layer.

4. Conclusion

SPS of pure Al powder was performed. Different pressures used during the process were 20, 30, 40 and 50 MPa. Final densities of the samples increased with pressure and reached near full density at 50 MPa. Ductility of the samples increased with pressure as observed with three-point bending tests. Resistance profiles indicate an enhanced decrease in resistance at 200 °C. This behavior is ascribed to breakdown of the oxide layer and an assessment methodology is presented to comment on the quality of the interface between Al particles. The results are consistent with the ductility and fracture surfaces of the samples.

Acknowledgments

The authors would like to acknowledge AUTO 21 (Grant No. C502-CPM) for their financial support and the Aluminum Research Centre—REGAL. The authors would also like to thank the Council of Higher Education of Turkey and Marmara University for scholarships to Mr. Tünçay.

References

1. X. Song, X. Liu, and J. Zhang, Neck Formation and Self-Adjusting Mechanism of Neck Growth of Conducting Powders in Spark Plasma Sintering, *J. Am. Ceram. Soc.*, 2006, **89**, p 494–500. doi:10.1111/j.1551-2916.2005.00777.x
2. Z.A. Munir, D.V. Quach, and M. Ohyanagi, Electric Current Activation of Sintering: A Review of the Pulsed Electric Current Sintering Process, *J. Am. Ceram. Soc.*, 2011, **94**, p 1–19. doi:10.1111/j.1551-2916.2010.04210.x
3. M. Omori, Sintering, Consolidation, Reaction and Crystal Growth by the Spark Plasma System (SPS), *Mater. Sci. Eng., A*, 2000, **287**, p 183–188. doi:10.1016/S0921-5093(00)00773-5
4. Z.A. Munir, Analytical Treatment of the Role of Surface Oxide Layers in the Sintering of Metals, *J. Mater. Sci.*, 1979, **14**, p 2733–2740. doi:10.1007/BF00610647
5. G. Xie, O. Ohashi, T. Yoshioka, M. Song, K. Mitsuishi, H. Yasuda, K. Furuya, and T. Noda, Effect of Interface Behavior Between Particles on Properties of Pure Al Powder Compacts by Spark Plasma Sintering, *Mater. Trans.*, 2001, **42**, p 1846–1849. doi:10.2320/matertrans.42.1846
6. T. Nagae, M. Yokota, M. Nose, S. Tomida, T. Kamiya, and S. Saji, Effects of Pulse Current on an Aluminum Powder Oxide Layer During Pulse Current Pressure Sintering, *Mater. Trans.*, 2002, **43**, p 1390–1397. doi:10.2320/matertrans.43.1390
7. G. Xie, O. Ohashi, K. Chiba, N. Yamaguchi, M. Song, K. Furuya, and T. Noda, Frequency Effect on Pulse Electric Current Sintering Process of Pure Aluminum Powder, *Mater. Sci. Eng., A*, 2003, **359**, p 384–390. doi:10.1016/S0921-5093(03)00393-9
8. G. Xie, O. Ohashi, M. Song, K. Furuya, and T. Noda, Behavior of Oxide Film at the Interface Between Particles in Sintered Al Powders by Pulse Electric-Current Sintering, *Metall. Mater. Trans. A*, 2003, **34**, p 699–703. doi:10.1007/s11661-003-0104-2
9. M. Zadra, F. Casari, L. Girardini, and A. Molinari, Spark Plasma Sintering of Pure Aluminium Powder: Mechanical Properties and Fracture Analysis, *Powder Metall.*, 2007, **50**, p 40–45. doi:10.1179/174329007x186417
10. H. Kwon, D. Park, Y. Park, J. Silvain, A. Kawasaki, and Y. Park, Spark Plasma Sintering Behavior of Pure Aluminum Depending on Various Sintering Temperatures, *Met. Mater. Int.*, 2010, **16**, p 71–75. doi:10.1007/s12540-010-0071-2
11. G.A. Sweet, M. Brochu, R.L. Hexemer, Jr., I.W. Donaldson, and D.P. Bishop, Microstructure and Mechanical Properties of Air Atomized Aluminum Powder Consolidated via Spark Plasma Sintering, *Mater. Sci. Eng., A*, 2014, **608**, p 273–282. doi:10.1016/j.msea.2014.04.078
12. N. Chawake, L.D. Pinto, A.K. Srivastav, K. Akkiraju, B.S. Murty, and R.S. Kottada, On Joule Heating During Spark Plasma Sintering of Metal Powders, *Scr. Mater.*, 2014, **93**, p 52–55. doi:10.1016/j.scriptamat.2014.09.003
13. A. Cincotti, A.M. Locci, R. Orrù, and G. Cao, Modeling of SPS Apparatus: Temperature, Current and Strain Distribution with No Powders, *AlChE J.*, 2007, **53**, p 703–719. doi:10.1002/aic.11102

14. D. Giuntini, E. Olevsky, C. Garcia-Cardona, A. Maximenko, M. Yurlova, C. Haines, D. Martin, and D. Kapoor, Localized Overheating Phenomena and Optimization of Spark-Plasma Sintering Tooling Design, *Materials*, 2013, **6**, p 2612–2632. http://www.mdpi.com/1996-1944/6/7/2612
15. P.D. Desai, H.M. James, and C.Y. Ho, Electrical Resistivity of Aluminum and Manganese, *J. Phys. Chem. Ref. Data*, 1984, **13**, p 1131–1172. doi:10.1063/1.555725
16. K. Vanmeensel, A. Laptev, J. Hennicke, J. Vleugels, and O. Vanderbiest, Modelling of the Temperature Distribution During Field Assisted Sintering, *Acta Mater.*, 2005, **53**, p 4379–4388. doi:10.1016/j.actamat.2005.05.042
17. X. Wei, D. Giuntini, A.L. Maximenko, C.D. Haines, and E.A. Olevsky, Experimental Investigation of Electric Contact Resistance in Spark Plasma Sintering Tooling Setup, *J. Am. Ceram. Soc.*, 2015, **98**, p 3553–3560. doi:10.1111/jace.13621
18. J.C.Y. Koh and A. Fortini, Prediction of Thermal Conductivity and Electrical Resistivity of Porous Metallic Materials, *Int. J. Heat Mass Transfer*, 1973, **16**, p 2013–2022. doi:10.1016/0017-9310(73)90104-X
19. J.M. Montes, F.G. Cuevas, and J. Cintas, Porosity Effect on the Electrical Conductivity of Sintered Powder Compacts, *Appl. Phys. A*, 2008, **92**, p 375–380. doi:10.1007/s00339-008-4534-y
20. N. Fuschillo, B. Lalevic, and B. Leung, Electrical Conduction and Dielectric Breakdown in Crystalline NiO and NiO(Li) Films, *J. Appl. Phys.*, 1975, **46**, p 310–316. doi:10.1063/1.321336
21. J.M. Montes, F.G. Cuevas, and J. Cintas, Electrical Resistivity of Metal Powder Aggregates, *Metal. Mater. Trans. B*, 2007, **38**, p 957–964. doi:10.1007/s11663-007-9097-3
22. T.B. Holland, U. Anselmi-Tamburini, D.V. Quach, T.B. Tran, and A.K. Mukherjee, Local Field Strengths During Early Stage Field Assisted Sintering (FAST) of Dielectric Materials, *J. Eur. Ceram. Soc.*, 2012, **32**, p 3659–3666. doi:10.1016/j.jeurceramsoc.2012.03.012
23. C.S. Bonifacio, T.B. Holland, and K. van Benthem, Time-Dependent Dielectric Breakdown of Surface Oxides During Electric-Field-Assisted Sintering, *Acta Mater.*, 2014, **63**, p 140–149. doi:10.1016/j.actamat.2013.10.018
24. J. McPherson, J.-Y. Kim, A. Shanware, and H. Mogul, Thermochemical Description of Dielectric Breakdown in High Dielectric Constant Materials, *Appl. Phys. Lett.*, 2003, **82**, p 2121–2123. doi:10.1063/1.1565180
25. E.M. Daver, W.J. Ullrich, and K.B. Patel, Aluminium P/M Parts—Materials, Production and Properties, *Key Eng. Mater.*, 1989, **29–31**, p 401–428
26. R.F. Tylecote, *The Solid Phase Welding of Metals*, St. Martin's Press, New York, 1968
27. S.C. Yoon, S.I. Hong, S.H. Hong, and H.S. Kim, Densification and Conolidation of Powders by Equal Channel Angular Pressing, *Mater. Sci. Forum*, 2007, **534–536**, p 253–256
28. M. Brochu, T. Zimmerly, L. Ajdelsztajn, E.J. Lavernia, and G. Kim, Dynamic Consolidation of Nanostructured A-7.5%Mg Alloy Powders, *Mater. Sci. Eng., A*, 2007, **466**, p 84–89. doi:10.1016/j.msea.2007.02.028
29. O. Yanagisawa, K. Matsugi, and T. Hatayama, Effect of Direct Current Pulse Discharge on Electrical Resistivity of Copper and Iron Powder Compacts, *Mater. Trans., JIM*, 1997, **38**, p 240–246. doi:10.2320/matertrans1989.38.240
30. E. Olevsky, I. Bogachev, and A. Maximenko, Spark-Plasma Sintering Efficiency Control by Inter-Particle Contact Area Growth: A Viewpoint, *Scr. Mater.*, 2013, **69**, p 112–116. doi:10.1016/j.scriptamat.2013.02.041
31. M.A. Meyers, A. Mishra, and D.J. Benson, Mechanical Properties of Nanocrystalline Materials, *Prog. Mater Sci.*, 2006, **51**, p 427–556. doi:10.1016/j.pmatsci.2005.08.003
32. K. Nishimoto, K. Saida, and R. Tsuduki, Effect of Pulsed Electric-Current on Densification Behavior of Bonded Interlayer of Oxide-Dispersion-Strengthened Superalloys Joint, *J. Jpn. Inst. Met.*, 2001, **65**, p 747–755